# Hindered Diffusion of High Molecular Weight Compounds in Brain Extracellular Microenvironment Measured with Integrative Optical Imaging

Charles Nicholson and Lian Tao
Department of Physiology and Biophysics, New York University Medical Center, New York, New York 10016 USA

ABSTRACT This paper describes the theory of an integrative optical imaging system and its application to the analysis of the diffusion of 3-, 10-, 40-, and 70-kDa fluorescent dextran molecules in agarose gel and brain extracellular microenvironment. The method uses a precisely defined source of fluorescent molecules pressure ejected from a micropipette, and a detailed theory of the intensity contributions from out-of-focus molecules in a three-dimensional medium to a two-dimensional image. Dextrans tagged with either tetramethylrhodamine or Texas Red were ejected into 0.3% agarose gel or rat cortical slices maintained in a perfused chamber at 34°C and imaged using a compound epifluorescent microscope with a 10 × water-immersion objective. About 20 images were taken at 2–10-s intervals, recorded with a cooled CCD camera, then transferred to a 486 PC for quantitative analysis. The diffusion coefficient in agarose gel, $D$, and the apparent diffusion coefficient, $D^*$, in brain tissue were determined by fitting an integral expression relating the measured two-dimensional image intensity to the theoretical three-dimensional dextran concentration. The measurements in dilute agarose gel provided a reference value of $D$ and validated the method. Values of the tortuosity, $\lambda = (D/D^*)^{1/2}$, for the 3- and 10-kDa dextrans were 1.70 and 1.63, respectively, which were consistent with previous values derived from tetramethylammonium measurements in cortex. Tortuosities for the 40- and 70-kDa dextrans had significantly larger values of 2.16 and 2.25, respectively. This suggests that the extracellular space may have local constrictions that hinder the diffusion of molecules above a critical size that lies in the range of many neurotrophic compounds.

## INTRODUCTION

Knowledge of the diffusion properties of brain extracellular microenvironment (BEM) is essential to understanding many mechanisms of brain function, as witnessed by the continued interest in extrasynaptic communication (Nicholson, 1979; Schmitt, 1984) or "volume transmission" (Fuxe and Agnati, 1991) and the obvious role of diffusion in delivering metabolic or therapeutic agents to brain cells (Nicholson and Rice, 1986). Many molecules that are candidates as extracellular signals or trophic factors are large in size, for example nerve growth factor is about 130 kDa (7S-NGF) and composed of several subunits each of about 26 kDa (Thoenen and Barde, 1980). While the importance of factors of high molecular weight in brain physiology is increasingly recognized (Fuxe and Agnati, 1991), little is known about the time course and spatial range of their actions, since adequate methods for the study of macromolecular diffusion in brain tissue have not been available.

During the last several years techniques have been developed for precisely determining the diffusion characteristics of small molecules in local regions of the brain using microiontophoresis or pressure microejection of tetramethylammonium combined with ion-selective microelectrodes (Nicholson and Phillips, 1981; Nicholson, 1992, 1993). This technique has been applied in a variety of preparations (Nicholson et al., 1979, 1993; Nicholson and Phillips, 1981; Nicholson and Rice, 1987; McBain et al. 1990; Svoboda and Syková, 1991; Cserr et al., 1991; Rice and Nicholson, 1991; Lundbæk and Hansen, 1992; Lehmenkühler et al., 1993; Rice et al., 1993). While the method is effective, it has two limitations 1) it provides a measurement at only a single point in the tissue so spatial patterns of diffusion are hard to determine 2) it can only be used with a few small ions ($\leq 100\,M_r$) due to the nature of ion-selective microelectrodes. In an earlier period of research on the BEM, radiotracers were the probe of choice and this permitted other compounds to be used (Fenstermacher and Patlak, 1975; Fenstermacher and Kaye, 1988), but since these studies relied on postmortem counting of particles in fixed and sectioned tissue they provided limited spatial resolution and no dynamic information.

To overcome the limitations of previous methods we have developed an optical technique that enables precise determination of the diffusion characteristics of fluorescently labeled compounds of high molecular weight. Because the optical signal arises from a diffusing cloud of molecules it is necessary to deal with signals from a continuum of depths in the preparation. To do this a method of integrative optical imaging was devised to solve the problem without the need to optically section the tissue. The method is based on a re-evaluation of the theory of out-of-focus images. A full theoretical description will be provided in another paper (Tao and Nicholson, submitted). Our approach differs from previous attempts to derive an apparent diffusion coefficient from digitized images (Wiederhielm et al., 1973; Nakamura and Wayland, 1975; Fox and Wayland, 1979; Aggarwal, 1989; Nugent and Jain, 1984a, b; Henry et al., 1992) in that we use a precisely defined source of fluorescent molecules,

*Received for publication 23 April 1993 and in final form 3 September 1993.*
Address reprint requests to Dr. Charles Nicholson at the Department of Physiology and Biophysics, New York University Medical Center, 550 First Avenue, New York, NY 10016.


0006-3495/93/12/2277/14 $2.00

and accurately account for the contribution of out-of-focus molecules to the image.

It is worth noting that we are dealing with a novel type of imaging problem. Normally a microscopist is concerned with the sharp rendition a two-dimensional structure in the in-focus object plane (even if a subsequent three-dimensional image is to be constructed), and this concern is exemplified by confocal microscopy. But here we are not concerned with sharpness, or even with an image in the conventional sense, we are instead simply mapping a cloud of photons into the memory of a computer. Because of this, many of the factors that limit conventional optics are of less significance to us. In this paper we first present and justify the method, then use it in dilute agarose gel and in rat cortical slices to determine the diffusion characteristics of dextran molecules as a function of molecular weight in control medium and in brain tissue. An abstract of this work has appeared (Tao and Nicholson 1992).

## Diffusion in the BEM

A given compound, characterized by a free aqueous diffusion coefficient $D$ ($cm^2\ s^{-1}$), diffuses in the BEM according to a generalization (Nicholson and Phillips, 1981; Nicholson, 1992) of the classic diffusion equation:

$$\frac{\partial C}{\partial t} = \frac{D}{\lambda^2}\nabla^2 C - \frac{f(C)}{\alpha} + \frac{Q(x, y, z, t)}{\alpha}. \quad (1)$$

Position is denoted by $(x, y, z)$ (cm) and time by $t$ (s), while $\nabla^2$ represents the second spatial derivative, and $C$ (mM) is the concentration of the diffusing molecules. A source-term $Q(x, y, z, t)$ (mM $s^{-1}$) describes local iontophoretic or pressure release of molecules. Uptake of material from the extracellular space, typically into cells, is defined by $f(C)$ (mM $s^{-1}$). If this function is zero or proportional to $C$ then Eq. 1 can be solved analytically for a variety of cases (Nicholson, 1992).

The generalized equation introduces two nondimensional factors, $\lambda$ and $\alpha$, that incorporate the structure of the tissue (Nicholson and Phillips, 1981). The first factor, $\lambda$, is the tortuosity, which accounts for the hindrance to extracellular diffusion that arises from the obstructions presented by cell membranes. Because of this hindrance we refer to an *apparent* diffusion coefficient, $D^*$, in tissue. Then $\lambda$ is defined by $\lambda = (D/D^*)^{1/2}$. The second structural factor, $\alpha$, is the volume fraction, which is simply the ratio of the volume of the BEM to the total volume of tissue averaged over some small reference domain.

# MATERIALS AND METHODS

## Organization of the experiment

Fig. 1 shows the experimental setup. Our optical imaging system consisted of a Zeiss Standard microscope equipped with a Nikon 10× water-immersion objective with NA of 0.3. Illumination was provided by a 100-watt tungsten-halogen epi-illuminator, powered by a DC stabilized power supply (Type 990017; LEP, Ltd., Hawthorne, NY), and a standard Zeiss

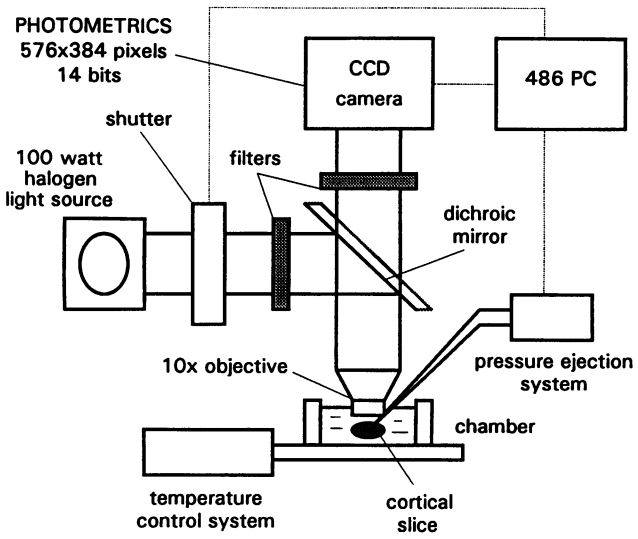


FIGURE 1 The IOI system, based on a Zeiss Standard compound microscope. The temperature-controlled recording chamber holds either agarose gel or a cortical brain slice. Fluorescent dextran molecules are ejected by pressure from a micropipette and diffuse through the sample. An epi-illumination system with suitable filters excites the dye molecules and the emitted signal is imaged directly on a cooled CCD camera using a 10× water immersion objective. The image recorded by the camera is transferred to a 486 PC. The computer controls the camera, the ejection system, and a shutter on the illumination source. See text for further details.

dichroic mirror system. The image was recorded by a CCD (charge-coupled device) camera cooled to −40°C (Model CH250; Photometrics, AZ) equipped with a Thompson CCD array with 576 × 384 pixels and 14-bit resolution. In the experiments described here only an area of 256 × 188 pixels was used so as to reduce the time required to transfer the image to the computer memory. The camera exposure time was 50 ms. To obtain maximum light efficiency the camera was attached to the microscope at the primary focus without any intermediate lens so that the objective formed a real image on the CCD chip. The output of the camera was transferred directly to the memory of a 486 PC. The computer also controlled a shutter (Uniblitz shutter and driver; Vincent Associates, Rochester, NY) on the illumination source, which was used to minimize photo-bleaching, and the computer controlled the dextran ejection system (described below). The software for data analysis and control of the equipment was written by Dr. Lian Tao and made use of the C Library supplied by Photometrics.

The brain slice chamber was mounted on the stage of the microscope using a custom-built assembly that permitted the independent or combined movement of the chamber and two micromanipulators mounted on either side. One manipulator held a microelectrode connected to a computer-controlled pressure ejection system to deliver a brief pulse of dextran to the preparation. The other manipulator held a stimulating electrode to evoke electrical activity from the brain slice. The temperature of the chamber was maintained at 34°C in all experiments by a custom-built Peltier device with a feedback system connected to a temperature probe in the bath.

For control experiments agarose gel was made by dissolving 0.3% agarose powder (NuSieve; FMC Corporation BioProducts, Rockland, ME) in 154 mM NaCl solution and heating while stirring until the solution became clear. The solution was then poured into the chamber and allowed to gel. This very dilute gel approximated a free solution but was not disturbed by thermal convection currents.

To prepare cortical slices, Sprague-Dawley rats of either sex (approximately 150 g) were anesthetized with sodium pentobarbital (60 mg/kg) and decapitated, and the brains were prepared for slicing as described elsewhere (Rice and Nicholson, 1991). Coronal slices were cut at 400-$\mu$m thick from the interaural 5–6-mm planes (Paxinos and Watson, 1986) and incubated at room temperature in physiological saline (see below). The slices were maintained in the sample chamber under physiological saline flowing at a rate

of about 1 ml/min by means of a peristaltic pump. The physiological saline had the following composition (in mM): NaCl 115; KCl 5; $NaHCO_3$ 35; $NaH_2PO_4$ 1.25; $MgCl_2$ 1.3; $CaCl_2$ 1.5; D-glucose 10; 0.2 sodium ascorbate; 0.2 thiourea (the latter two compounds were used as antioxidants (Rice and Nicholson, 1991)). The solution was gassed continuously with 95% $O_2$-5% $CO_2$ to provide a pH of 7.5. In some experiments the viability of the slices was checked by local stimulation through a bipolar-twisted wire electrode which evoked local field potentials that were measured with a conventional microelectrode, amplifier, and oscilloscope. The diffusion measurements were made in cortical layers III, V, and VI but no significant differences in the results for different layers were noted.

The ejecting microelectrode, with tip diameter of 3–5 $\mu$m and containing an appropriate fluorescent dextran, was inserted into the slice at an angle of 30° with respect of the surface until the tip was in the middle of the slice (i. e., at a depth of about 200 $\mu$m). The electrode was connected to a nitrogen pressure source of 10–30 p.s.i. through a computer-controlled fast-vent valve (General Valve, Fairfield, NJ) with typical opening duration of 100–200 ms. The ejection pressure and duration were adjusted so that the volume of ejected dye was appropriate for the sensitivity and dynamic range of the CCD camera. We did not routinely measure the quantity of dextran ejected, but, in some experiments where the optical method was combined with simultaneous tetramethylammonium measurements, we estimated a typical release volume of 1 nl or less. After each ejection, a set of about 20 successive images was taken to record the diffusion process. The time interval between two successive images varied from 2 to 10 s, depending the molecular weight of the dextran and, therefore, its rate of dissipation. After acquisition, the images were processed and analyzed to extract the diffusion parameters as described below.

### Choice of probe molecules and fluorescent tags

To study how large molecules move through the BEM we selected fluorescent dextrans, for two major reasons. First, because there is precedent for the use of such molecules to study diffusion in biological systems (e.g., Fox and Wayland, 1979; Nugent and Jain 1984a, b; Luby-Phelps et al., 1986; Järnfelt et al., 1988; Aggarwal, 1989; Henry et al., 1992). Second, the structural properties of dextrans in solution have been investigated (Ogston and Woods, 1953; Granath, 1958; Granath and Kvist, 1967). Dextrans are neutral molecules that only acquire charge groups from the fluorescent molecules used to label them and are also very water-soluble. Consequently dextrans do not interact significantly with membranes. Although dextrans are flexible, branched random-coil structures that do not necessarily conform closely to a rigid sphere (Luby-Phelps et al., 1986), studies on the cytoplasm of 3T3 cells have shown that dextrans behave in a similar way to Ficoll molecules which do have a hard-sphere configuration (Luby-Phelps et al., 1987).

Because the CCD that we used had 30–40% efficiency in the red wavelengths and much lower performance toward the blue, we used dextrans tagged with red fluorophores. This choice had the further advantage that a tungsten-halogen illuminator was adequate and this was easier to stabilize than a mercury arc. We used dextrans with molecular weights of 3, 10, 40, and 70 kDa (Types D3307, D1828, D1829, and D1830, respectively; Molecular Probes, Eugene, OR,). The 3-kDa dextrans were tagged with tetramethylrhodamine (absorption maximum, 555 nm; emission maximum, 580 nm (Haugland, 1992)) and used at a concentration of 1 mM, dissolved in 154 mM NaCl solution. The other dextrans were all tagged with Texas Red (absorption maximum, 591 nm; emission maximum, 612 nm (Haugland, 1992)) and used at a concentration of 100 $\mu$M in 154 mM NaCl solution. For tetramethylrhodamine we used a Zeiss filter set that allowed excitation wavelengths of 510–560 nm, a beam splitter (dichroic mirror) at 580 nm and a barrier at 590 nm. For Texas Red we used excitation wavelengths of 530–585 nm, a beam splitter at 600 nm, and barrier filter at 615 nm. Since the diffusion properties of the dyes began to change after being in solution for a few days at room temperature, fresh solutions were made for each experiment.

## THEORY

To obtain the diffusion parameters of molecules moving in a tissue it is necessary to measure the temporal and/or spatial distribution of the molecules. Using the optical systerm described above, however, the *direct* measurement of the molecular distribution in a three-dimensional sample is difficult. Due to the diffraction of light, a point source does not generate a point image, even if the point is in focus. Instead, a set of concentric rings, called the Airy pattern (Born and Wolf, 1986), is generated. Furthermore, in a three-dimensional sample, the fluorescent molecules in the out-of-focus planes also contribute to the image intensity. Thus, in principle, the intensity of each point in the image plane of the CCD has contributions from the whole sample and there is no simple one-to-one correspondence between the intensity of a point in the image plane and a point in the sample volume. Accordingly one cannot simply fit the recorded image with the theoretical expression for the distribution.

The derivation of the three-dimensional concentration from its two-dimensional image constitutes an inverse problem, which in general has no unique mathematical solution. In principle one can partially solve this problem by taking several images at different depths and then using appropriate algorithms to remove the blurring produced by out-of-focus molecules (Agard, 1984; Yae et al., 1992) to find the approximate concentration in the focal plane. In this method, a set of images at different depths must be recorded making it necessary to mechanically move the microscope stage, or the focusing system. This slows the sampling procedure and the concentration distribution may change significantly during the data acquisition so that data analysis becomes complex.

### Integrative optical imaging

Here we implement another approach that we call Integrative Optical Imaging (IOI). We record a single two-dimensional image of a three-dimensional concentration, using the fluorescent microscope system described above. This image contains not only the signal from the in-focus plane, but also from the out-of-focus planes. Rather than trying to extract the concentration from the image we fitted the recorded image with a theoretical expression for the image to be expected from a collection of molecules diffusing away from a point source. From this fitting we obtain the diffusion parameters.

### The defocused point-spread function

The image of a three-dimensional incoherent light source formed by an aberration-free optical system with linearity and shift-invariance is a convolution of the object with the defocused point-spread function (DPSF) (Castleman, 1979). To a good approximation, a modern microscope objective of low numerical aperture (NA $< 0.5$) can be treated as an aberration-free system with linearity and shift-invariance. Moreover, when such a low-NA lens is used in epifluorescent

mode, the illumination is essentially constant over the effective depth of field, to be calculated below. Note that high-NA objectives (NA > 1.0) suffer from both significant aberrations and may produce a a partial confocal behavior because of their illumination properties (Hiraoka, 1990), but these issues are not relevant to the objective used in the present studies.

The fluorescent molecules in the sample constitute a three-dimensional incoherent light source. For such an ideal optical system, the two-dimensional image $I(x', y')$ of a three-dimensional incoherent light source $C(x, y, z)$ is given by the following integral:

$$I(x', y') = \int\int\int_{\text{sample space}} C(x, y, z)S(x' - Mx, y' - My; z)\, dx\, dy\, dz. \quad (2)$$

In this paper the nonprimed letters denote variables in the object space, while the primed letters denote variables in the image space. The integration is carried out over the whole sample space, i. e., the space occupied by the sample. $M$ is the magnification of the objective. The function $S(x' - Mx, y' - My; z)$ is the DPSF, which weights the contribution from a source point located at $(x, y, z)$ in the sample to the image point $(x', y')$.

By definition, the DPSF, $S(x', y'; z)$, is the image intensity of a point source located on the optical axis ($x = 0 = y$) with a displacement $z$ from the in-focus plane. For an optical system with circular symmetry, the DPSF has the following form (Tao and Nicholson, submitted):

$$S(x', y'; z) = S(r'; z) = \left\{\frac{2}{M}\int_0^1 \cos(kW'\rho^2)J_0(u'\rho)\rho\, d\rho\right\}^2 + \left\{\frac{2}{M}\int_0^1 \sin(kW'\rho^2)J_0(u'\rho)\rho\, d\rho\right\}^2 \quad (3)$$

where $W' = -R' - z'\cos\theta' + (R'^2 + 2R'z' + z'^2\cos^2\theta')^{1/2}$ (Stokseth, 1969), $R' = L(M + 1)/M$, $L$ = optical tube length of the microscope, $\theta' = \tan^{-1}(R_{\text{pupil}}/R')$, $R_{\text{pupil}} = nR'/M)\tan\theta$, $n$ = refractive index of object space, $NA$ = numerical aperture of objective, $z' = LM^2z/(nL + M^2z)$, $k = 2\pi/\lambda_w$, $\lambda_w$ = wavelength in vacuum, $J_0(q)$ = Bessel function of first kind and zero order, $u' = kr'/R'$, $r' = (x'^2 + y'^2)^{1/2}$. In Eq. 3 all the lengths are expressed in such a unit that the radius of the effective exit pupil of the objective, $R_{\text{pupil}}$, is unity: before evaluating the expression, it is necessary to convert all the lengths into such units.

To examine the DPSF on the in-focus plane, we set $z = 0$ in Eq. 3 and carry out the integration. The expression reduces to

$$S(r'; z = 0) = \left\{\frac{2J_1(u')}{Mu'}\right\}^2, \quad (4)$$

where $J_1(u')$ is the Bessel function of the first kind and first order. This is a well known result (Born and Wolf, 1986) for the in-focus point-spread function.

As an example, the DPSF $S(r', z)$ of our IOI system ($M = 10$, $NA = 0.3$, $L = 160$ mm, $n = 1.33$, and $\lambda_w = 610$ nm) has been computed using Eq. 3 and plotted in Fig. 2. In the figure, each curve presents the DPSF at a different $z$ distance from the in-focus plane. We can see that only the curves representing slightly out-of-focus image planes have large amplitudes, and these curves tend to become zero after

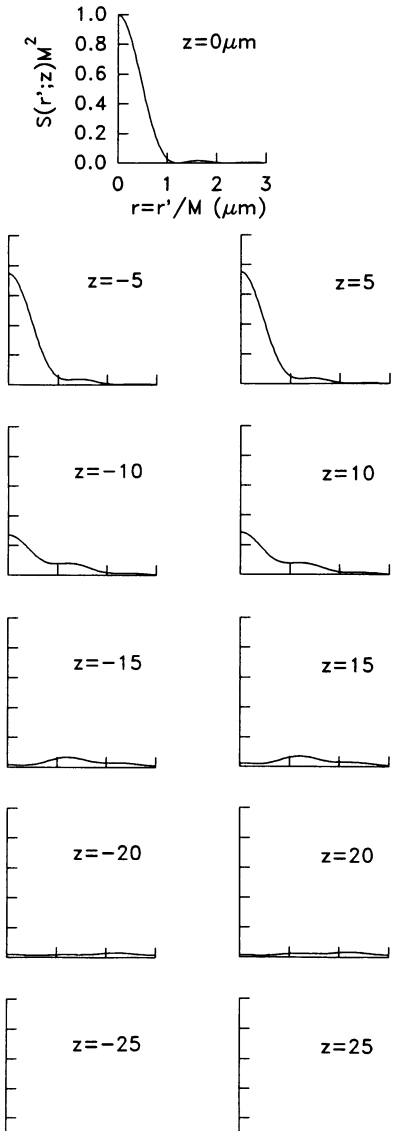


FIGURE 2 The DPSF $S(r'; z)$ of the IOI system. The DPSF is based on the following objective parameters: $M = 10$, $NA = 0.3$, $L = 160$ mm, $n = 1.33$, and $\lambda_w = 610$ nm. Each curve presents the DPSF at a different defocusing and all the plots use the same units. The radius in the image space, $r'$, has been converted into the radius in the object space, $r$, to visualize the effective radius of the field. Only the curves of small defocusing have large amplitudes and these tend to become zero after their first minimum. The first minimum of the in-focus ($z = 0$ μm) curve occurs at $r_e$, which is defined as the effective radius of the field.

their first minimum. The minima for the curves of out-of-focus planes occur at about the same radius as the in-focus curve. From Eq. 4, the first minimum of the in-focus curve occurs at the radius where the equation $J_1(u')$ has its first root, namely $u' = kr'/R' = 1.22\pi$. The corresponding radius is $r'_e = 1.22\pi R'/k$. Since $r'_e$ is the radius in the image space, it can be converted into the radius in the object space $r_e$ by the simple relation $r_e = r'_e/M$.

Since only the light sources located within a radius $r_e$ of a point in the sample space make a significant contribution to the corresponding image point, the parameter $r_e$ can be defined as the effective radius of the field. For our IOI system $r_e$ is about 1.37 $\mu$m.

To examine the DPSF along the axis, we set $r' = 0$ in Eq. 3 and carry out the integration. The expression reduces to

$$S(r' = 0; z) = \left\{ \frac{\sin(kW'/2)}{MkW'/2} \right\}^2. \quad (5)$$

This is an even function with respect to $W'(z)$ but not with respect to $z$. As we have shown (Tao and Nicholson, submitted) for small $z$, we have $W'(z) = az$, where $a = (M^2/2n) \sin^2 \theta'$. Then Eq. 5 can be written as

$$S(r' = 0; z) = \left\{ \frac{\sin(kaz/2)}{Mkaz/2} \right\}, \quad (6)$$

which is an even function with respect to $z$.

For our IOI system, the DPSF along the $z$ axis has been computed using Eq. 6 and plotted in Fig. 3. In the figure we see that the curve $S(r' = 0; z)$ tends to become zero after its first minimum. From Eq. 6, the first minimum of $S(r' = 0; z)$ occurs when the equation $\sin(kaz/2) = 0$ has its first root. The corresponding values of $z$ are $\pm z_e = \pm 2\pi/ka$.

Since only the sources located between $-z_e$ and $z_e$ have significant weights, the value $z_e$ defines the effective depth of field which, for our IOI system, is about 17.1 $\mu$m.

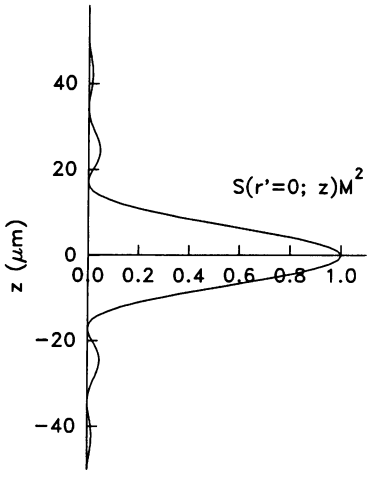


FIGURE 3 The DPSF along the axis, $S(r' = 0; z)$, of the IOI system. The curve tends to become zero after its first minimum which occurs at $\pm z_e$, which is defined as the effective depth of field.

In summary: any objective has an effective radius of field $r_e$ and an effective depth of field $z_e$, these two parameters together define an effective cylinder of field in the object space. Only light sources located within the effective cylinder contribute significantly to the corresponding image point. The effective cylinder is shown in Fig. 4.

## Theoretical concentration distribution after pressure ejection from a point source

For a given concentration, the image intensity can be computed using Eq. 2. The actual form of the concentration $C(x, y, z)$ depends on how the diffusing molecules are ejected into the sample and the composition of the sample. In this paper we only consider the case where the molecules are ejected by pressure into a homogeneous and isotropic sample. We also assume that the large molecules considered here do not leave the extracellular space, so that there is no uptake i. e., $f(C) = 0$ in Eq. 1. We assume that the volume $U$ (liters) of material injected at concentration $C_f$ (mM) is sufficiently small that the molecules can be regarded as diffusing from a point source and forming a distribution with spherical symmetry. If we write $\gamma^2 = 4D^*t$ (cm$^2$) then the extracellular concentration distribution is (Nicholson, 1985; 1992)

$$C^o(x, y, z, \gamma) = \frac{UC_f}{\alpha(\gamma\sqrt{\pi})^3} e^{-(x^2+y^2+z^2)/\gamma^2}. \quad (7)$$

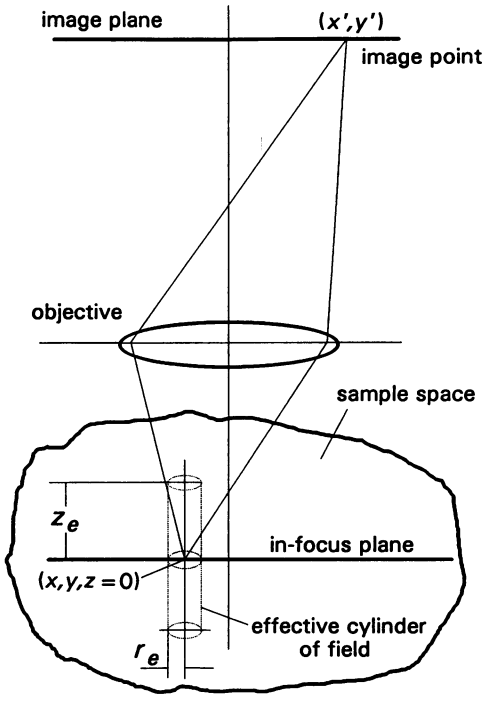


FIGURE 4 The effective cylinder of the field. For a given image point only the light sources located within the effective cylinder with radius $r_e$ and length $2z_e$, make a significant contribution.

Here we have used the nomenclature $C^o$ to indicate that the concentration designated by Eq. 7 is defined with respect to the extracellular phase alone, which is the quantity that is measured with an ion-selective microelectrode or similar sensor inserted into brain tissue. But the sample space implicit in the integral defined in Eq. 2 is taken over the whole tissue volume phase. To reconcile these two quantities we note that

$$C(x, y, z, \gamma) = \alpha C^o(x, y, z, \gamma). \tag{8}$$

This point is discussed in more detail elsewhere (Nicholson and Phillips, 1981; Nicholson, 1985). A consequence in the present approach is that the volume fraction ($\alpha$) cannot appear in the final expression for $I(x, y, \gamma)$, so it cannot be obtained from the curve fitting. This is a result of the integrative nature of the method, in contrast to microelectrode techniques that sample the BEM in the vicinity of a point.

Substituting Eqs. 3, 7, and 8 into Eq. 2, one can compute the image intensity for any given $\gamma$. Since the contribution $C(x, y, z)$ posses spherical symmetry, and as long as $z \ll R$ the DPSF is almost symmetric about the $z = 0$ plane, we need only carry out the integration in the ¼ space of $y \geq 0$ and $z \geq 0$, and multiply the result by 4 to get the correct image intensity.

## Approximations to the DPSF

While the DPSF in Eq. 3 is more rigorous than the subsequent approximations, it requires numerical computation of the integrals. Using this DPSF in the integrand of Eq. 2 will result in a fourfold integral. In order to fit the measured image intensity, all the fitting parameters will be adjusted many times. Each time a parameter is adjusted, this fourfold integral will have to be computed and it may take a typical 486 computer many hours to find a set of best-fitting parameters. Obviously this is too slow for practical use and we need to find an approximation that will permit curve-fitting in a realistic period of time.

Since the DPSF has a very small effective radius, compared to the dimension of the sample, and a relatively large effective depth, we suggest here an approximate expression for the DPSF, which reduces the computation dramatically. The approximation has the following form

$$\begin{aligned} S(x', y'; z) &\approx AK\delta(x', y')S(r' = 0; z) \\ &= AK\delta(x', y')\left\{\frac{\sin(kaz/2)}{kaz/2}\right\}^2 \end{aligned} \tag{9}$$

where $\delta(x', y')$ is the two-dimensional Dirac delta function, and is used here to describe the $x'$ and $y'$ dependencies of the DPSF. That means that all the point sources along a line parallel to the principal optical axis contribute to the same point in the image plane, and all the point sources off the line do not make any contribution to this image point. The function $S(r' = 0; z)$ is the DPSF along the $z$-axis, which is used here to weight the contributions of the point sources along the line. The constant $K$ normalizes the approximate DPSF so that it can generate the same image intensity as the one produced by the rigorous DPSF for $C(x, y, z, \gamma) = 1$, i.e.,

$$\begin{aligned} &\int_{\text{sample space}}\int\int S(Mx, My; z)\, dx\, dy\, dz \\ &= K\int_{\text{sample space}}\int\int \delta(Mx, My)S(r' = 0; z)\, dx\, dy\, dz. \end{aligned} \tag{10}$$

Using this approximate DPSF, Eq. 2 becomes

$$\begin{aligned} I(x', y', \gamma) = AK\int_{\text{sample space}}\int\int C(x, y, z, \gamma) \\ \delta(x' - Mx, y' - My)S(r' = 0; z)\, dx\, dy\, dz. \end{aligned} \tag{11}$$

The entire optical system, including the CCD camera, will have a calibration factor $A$ that relates intensity to the values appearing in the computer memory; this factor will be measured using a source of known intensity.

We are able to use $S(r' = 0; z)$ at locations for which $r' \neq 0$ due to the property of shift invariance that we have assumed for the optical system. Then using the formal properties of the delta function, Eq. 11 reduces to

$$I(x', y', \gamma) = \frac{AK}{M^2}\int C\left(\frac{x'}{M}, \frac{y'}{M}, z, \gamma\right)S(r' = 0; z)\, dz. \tag{12}$$

Inserting Eqs. 7, 8, and 9 into Eq. 12, we have

$$\begin{aligned} &I(r', \gamma) \\ &= \left\{\frac{AKUC_f}{M^2(\gamma\sqrt{\pi})^2}\int\left[\frac{\sin(kaz/2)}{kaz/2}\right]^2 e^{-(z/\gamma)^2}\, dz\right\} e^{-(r'/M\gamma)^2}. \end{aligned} \tag{13}$$

To emphasize the specific dependence of the image $I(r', \gamma)$ on $r'$ we write this as

$$I(r', \gamma) = E(\gamma)e^{-(r'/M\gamma)^2}. \tag{14}$$

Using Eq. 13, the theoretical image intensity can be computed by a single integration, instead of a fourfold integration with consequent reduction in computation time. In order to see how much error has been introduced into the computed image by using the approximate DPSF, we have computed the image intensity using Eq. 13 and plotted the results in Fig. 5 for comparison with the intensity computed with rigorous DPSF (Eqs. 2, 3, 7, and 8). From Fig. 5 we see that for $\gamma < r_e$, using the approximate DPSF to compute the image will result in large errors. For $\gamma > 10\ r_e$, the images computed using the approximate DPSF (Eq. 9) and using the accurate DPSF (Eq. 3) are essentially the same. In our study $\gamma > 20\ r_e$ at all times so, the approximate DPSF is perfectly adequate. Therefore we have used Eq. 14 as our the theoretical image intensity in the fitting procedure.

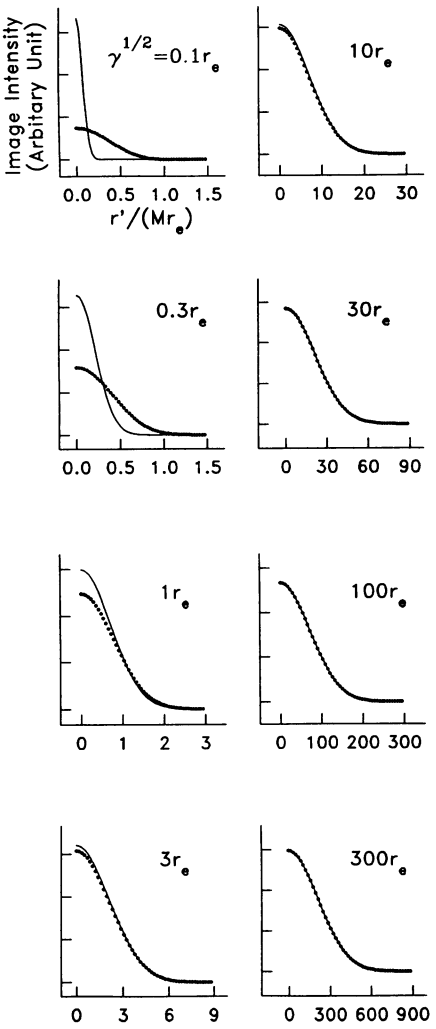


FIGURE 5 The theoretical image intensity. Each plot presents the image intensity at a different value of $\gamma$ and uses a different scale for the intensity axis. The spatial axes use a rational unit $r'/(Mr_e)$, with different scales as indicated. The dotted lines are the image intensities computed using the accurate DPSF, Eq. 3, while the solid lines are the intensities computed using the approximate DPSF, Eq. 9. For $\gamma < r_e$, using the approximate DPSF to compute the image will result in large errors. For $\gamma > 10r_e$, the images computed using the approximate DPSF and using the accurate DPSF are essentially the same.

### Determining the apparent diffusion coefficient using the whole set of images

In the following we describe the extraction of $D^*$ in a tissue slice, the procedure for obtaining $D$ in agarose is, of course, identical. Data is obtained by taking images at a sequence of times $t_i$. In these experiments we assume that $D^*$ is a constant for a given tissue and molecular species, so for any given image there is a $\gamma_i^2 = 4D^*t_i$ which is constant, hence from Eq. 13 $E(\gamma)$ will also be constant for that image and $\gamma_i$ can be obtained by fitting the spatial variation in Eq. 14 to the measured intensity distribution

$$I_i(r, \gamma) = E_i e^{-(r/\gamma_i)^2}. \quad (15)$$

Here we write the exponent in terms of $r$ rather than $r'$ because our practical measurements relate exclusively to the sample space and measurements on the image are always calibrated with respect to known distances in the sample space. We note that, although $E_i$ is a function of $\gamma_i$, we do not need to make use of that fact to obtain $\gamma_i$ in this study. This is equivalent to ignoring the absolute amplitude information as a function of time, which is justified by the complexity of $E$, involving as it does the need for numerical integration. Another advantage is that we do not need to calibrate the image intensity, we merely have to maintain constant illumination during the image acquisition process. If the intensity were calibrated in terms of a concentration standard then we would be able to make use of the additional information in $E$ and further information could be extracted from the image, such as the volume of dextran ejected.

We do, however, make use of the temporal information in the sequence of images in the following way. First we recognize that there is uncertainty about the exact time when the measurements begin due to the fact that the initial pulse of dextran delivered to the tissue is brief ($< 1$ s) but still of finite duration and there is a subsequent period during which the dextran infiltrates the extracellular space of the tissue. It has also been pointed out recently (Basser, 1992) that the simple formulation embodied in Eq. 7 does not explicitly satisfy basic laws of mechanics that would incorporate the elasticity of the tissue. We can allow for these temporal uncertainties by supposing that the apparent origin in time of the diffusion process is at time $t_0$ before our actual time measurements commence so that we should write

$$\gamma_i^2 = 4D^*(t_i + t_0). \quad (16)$$

We then used a two-stage strategy to extract $D^*$. First, for each time at which we have a concentration distribution, i.e., at times $t_1$, $t_2$, $t_i \cdots t_n$ we fit Eq. 15 using the nonlinear Levenberg-Marquandt algorithm (Press et al., 1986). This yields a sequence of estimates of $\gamma_i$ as a function of the $t_i$. The second step is to perform a linear regression on these data to extract $D^*$ using Eq. 16. In this way the entire sequence of images are used to refine the estimate of $D^*$.

Finally we note that, in order to deal with any constant background fluorescence, an image can be recorded before each dextran ejection. This background signal is then subtracted from the images taken after the ejection when the images are subsequently analyzed.

## RESULTS

### Diffusion of dextrans in agarose

Measurement of $D$ for the four dextrans in dilute agarose gel provided a validation of the IOI method and essential reference data for the determination of $\lambda$ in brain tissue.

Results for the diffusion of 3-kDa dextran are shown in Fig. 6. After the dextran solution was pressure-ejected into the agarose gel, 16 images were recorded successively with a time interval of 2 s. The four images shown in the figure were recorded at 4, 8, 16, and 32 s after the ejection. As expected, these images possess spherical symmetry about the

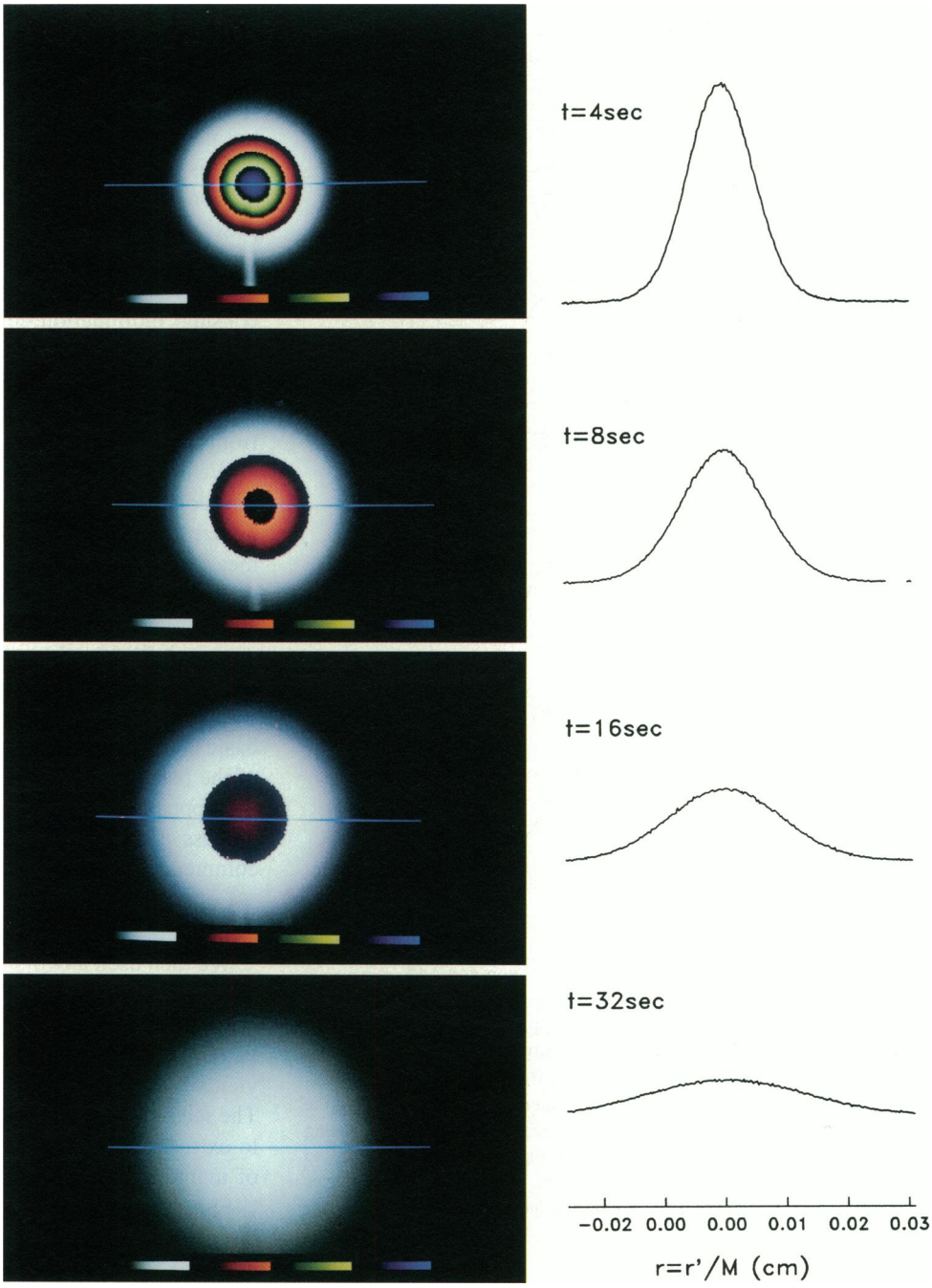


FIGURE 6 The diffusion of 3-kDa dextrans in agarose gel. After the 3-kDa dextran solution was injected in the agarose gel, 16 images were recorded successively with a time interval of 2 s. The four images shown here were recorded at 4, 8, 16, and 32 s after the nominal time of injection and displayed in pseudo-colors. The color coding of the image intensity is such that white represents the lowest intensity and blue the highest, as indicated by the color bar in the figure. These images possess spherical symmetry about the injection point, reflecting the homogeneity and isotropism of agarose gel. The intensity profile along the horizontal line intersecting the injection point in each image is plotted on the right.

ejection point, since the gel is homogeneous and isotropic. The intensity profile along a horizontal line passing through the ejection point in each image is plotted beside the image.

Using the two-step fitting procedure, we extracted the value of $D$. On the left of Fig. 7 *a*, we plot the intensity curves of images taken at 4, 8, 12, 16, 24, and 32 s with the best-fitting theoretical curves (Eq. 15) superimposed. It is evident that the theoretical curves give a virtually perfect fit. The values of $\gamma_i^2/4$ obtained at each time are plotted in the right-hand panel for this experiment. From the slope, $D$ can be obtained (Eq. 16). It is apparent that the line intersects the time axis slightly to the left of the origin, i.e., $t_0$ has a small negative value.

Fig. 7, *b–d*, show the results of similar curve fitting for the diffusion of the 10-, 40-, and 70-kDa dextrans in agarose. These three curves, together with the one depicted in Fig. 7 *a*, all fit with similar precision and the value of $t_0$ is slightly negative in all cases.

Experiments like the ones depicted in Figs. 6 and 7 were repeated about eight times for each type of dextran. The means and the standard deviations of the measured diffusion coefficients are given in Table 1.

## Diffusion of dextrans in rat cortical slices

Our ultimate goal was to investigate how large molecules move through the BEM of the cerebral cortex. To this end we studied the diffusion of the four fluorescent dextrans of different molecular weights in slices of rat cerebral cortex, using the same methods as described for agarose. Fig. 8

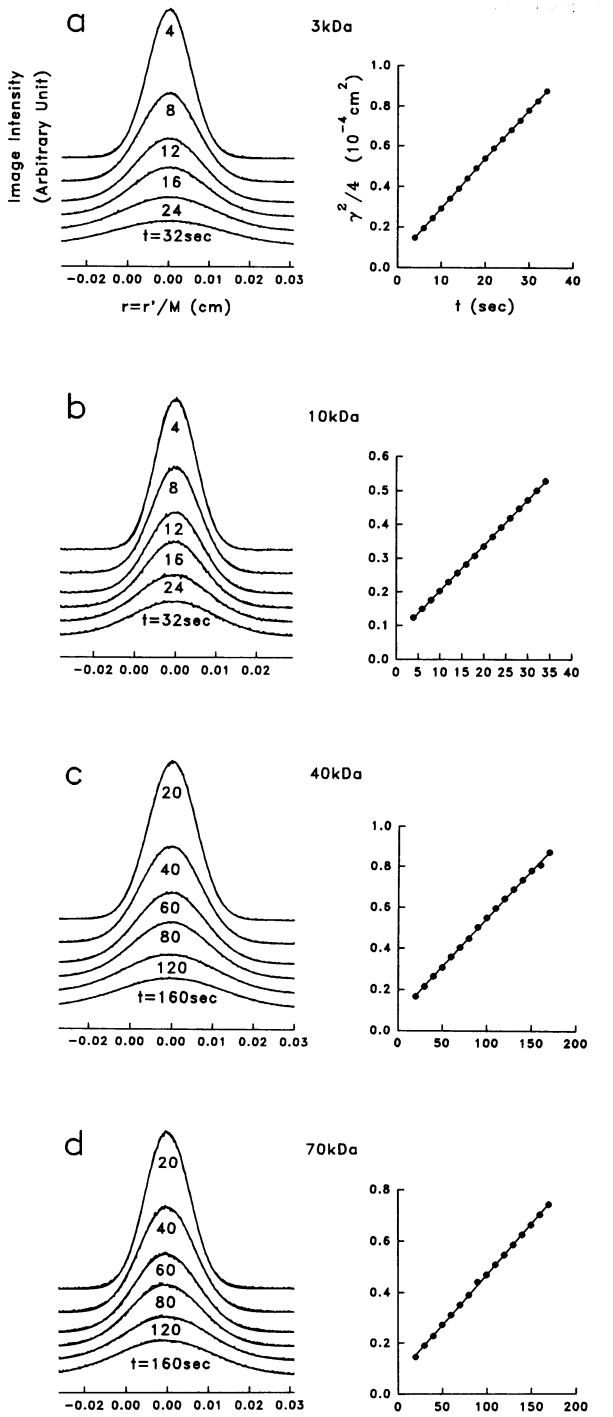


FIGURE 7 Diffusion profiles in agarose gel. *a*, *b*, *c*, and *d*, show the diffusion profiles, taken through the ejection point, of the 3-, 10-, 40-, and 70-kDa dextrans, respectively. On the left of each panel are six intensity curves, which are among the series of 16 images taken after each ejection, with their best-fitting theoretical curves (Eq. 15) superimposed. From fitting the intensity curve of the image taken at time $t_i$ we obtained the function value $\gamma_i$. The 16 function values $\gamma_i^2/4$ vs. time $t_i$ are plotted on the right with a best-fitting regression line. The slope of the straight line gives the required apparent diffusion coefficient, $D^*$, using Eq. 16.

shows the diffusion of the 3-kDa dextrans in a slice following pressure ejection. The four images shown in the figure again were recorded at 4, 8, 16, and 32 s after the ejection. These images demonstrate the spherical symmetry about the ejection point, perturbed only by the shadow of the injecting microelectrode as it entered the tissue obliquely under the microscope objective. The intensity profile along a horizontal line through the ejection point in each image is plotted on the right of the figure.

**TABLE 1 Diffusion parameters for dextrans in agarose and brain**

| Dextran | Agarose gel | Cortical slice | Tortuosity |
|---|---|---|---|
| $M_r$ kDa | $D$ ($10^{-7}$ cm$^2$ s$^{-1}$) | $D^*$ ($10^{-7}$ cm$^2$ s$^{-1}$) | $\lambda = (D/D^*)^{1/2}$ |
| 3 | 23.3 ± 2.1 (8) | 8.1 ± 0.4 (9) | 1.70 ± 0.04 |
| 10 | 13.5 ± 0.9 (11) | 5.1 ± 0.7 (10) | 1.63 ± 0.05 |
| 40 | 4.2 ± 0.3 (8) | 0.91 ± 0.21 (8) | 2.16 ± 0.11 |
| 70 | 3.8 ± 0.2 (8) | 0.75 ± 0.16 (12) | 2.25 ± 0.09 |

Errors for $D$ and $D^*$ are standard deviations. Number of observation in parentheses. Errors for $\lambda$ are calculated as $\pm 0.5\lambda(D_{s.e.m.}/D + D^*_{s.e.m.}/D^*)$, where $D_{s.e.m.}$, $D^*_{s.e.m.}$ are the standard errors of the means.

Again the two-step analysis process was applied to the data (Fig. 9). The theoretical curve (Eq. 15) fitted well, but some deviation was evident at the peak and on the falling shoulders of the curves. The deviation at the peak was probably due to tissue elasticity (Basser, 1992) or other factors that were only relevant in the immediate vicinity of the ejection site. The deviation on the shoulders is presently not accounted for, but neither deviation was enough to be very significant. The values of $\gamma_i^2/4$ plotted as a function of time are reasonably fitted by straight lines, so that a reliable estimate of $D^*$ (Eq. 16) was obtained, although there was more scatter as the size of the dextrans increased. Again, in all cases, $t_0$ had a negative value but became quite large for the bigger molecules.

The means and the standard deviations of the values of $D^*$ are given in Table 1 together with the corresponding tortuosity values ($\lambda = (D/D^*)^{1/2}$). It is evident that the values of $\lambda$ for the two smaller dextrans were similar but that $\lambda$ increased for the two larger molecules.

## DISCUSSION

### Integrative optical imaging

Several previous studies have obtained estimates of the apparent diffusion coefficient of large fluorescent molecules from digitized images. The approach was demonstrated in an early paper by Wiederhielm et al. (1973) using a nonfluorescent dye, video camera, and microscope to study diffusion in the vicinity of a capillary bed. More elaborate studies in capillary beds and mesentery tissue of rats, using fluorescein isothiocyanate, fluorescent dextrans, and fluorescent bovine serum albumin were carried out by Nakamura and Wayland (1975) and Fox and Wayland (1979). A further study of microvascular permeability and local diffusion in normal and burn tissue was made by Aggarwal et al. (1989). Perhaps the most precise experiments of this type were carried out by Nugent and Jain (1984a, b) in normal and neoplastic tissues. In a recent study, using the image approach, Henry et al. (1992) exposed the end of a tube of gel to a constant concentration of fluorescent dextrans. Such an approach, however, is unsuitable for brain tissue.

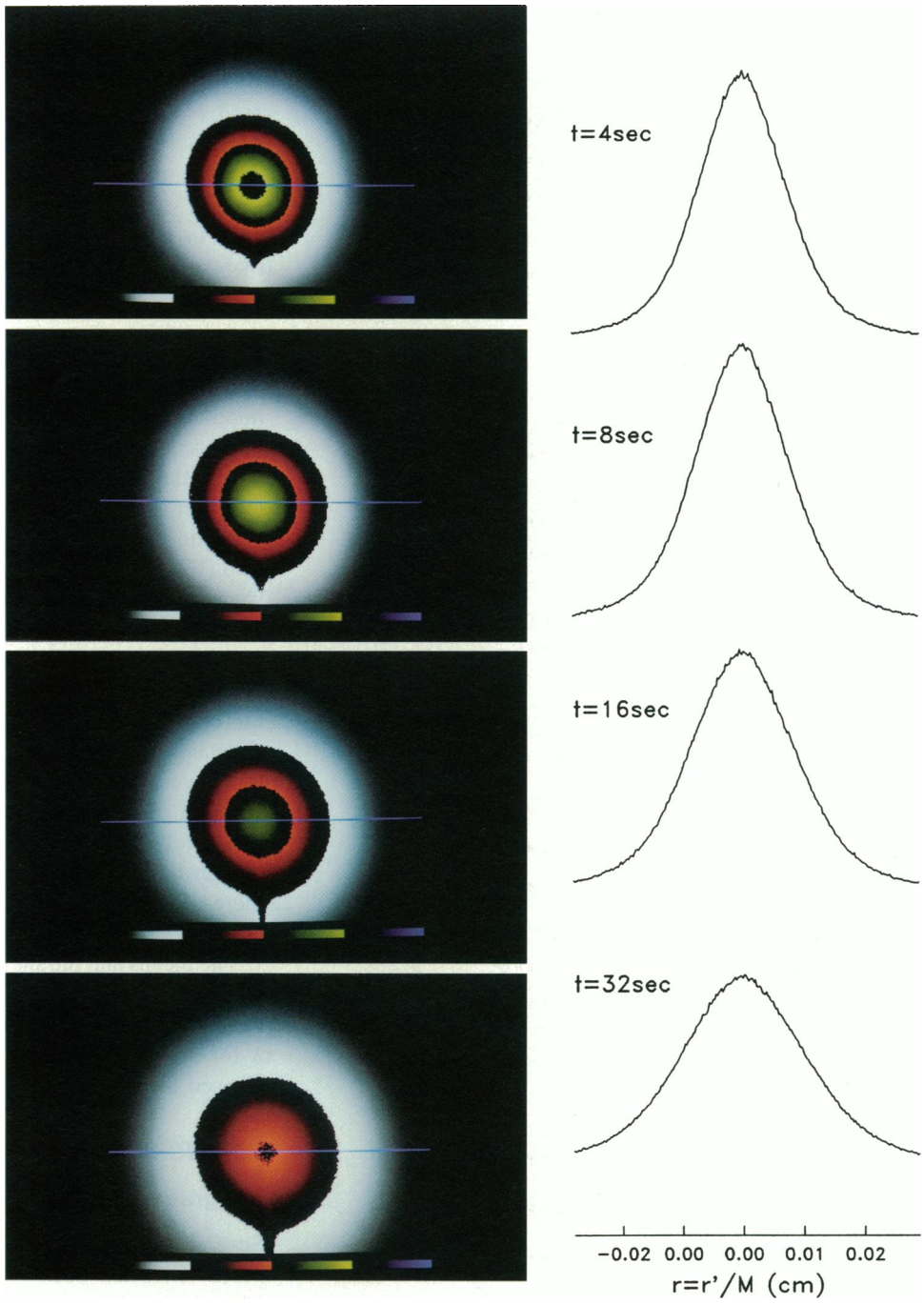


FIGURE 8 The diffusion of 3-kDa dextrans in cortical slices. These data were obtained in the same way as those shown for the agarose gel in Fig. 6. Note the spherical symmetry and clarity of the images in the brain slices. The shadow of the injecting microelectrode is apparent in some of the images.

The previous studies in tissue sought to image fluorescent molecules as they diffused away from the vicinity of blood vessels. The complicated geometry of the source and inability to precisely characterize the emitted flux, substantially limited the quality of the results.

An optical method that provides a better defined source is Fluorescent Recovery After Photobleaching (FRAP) where a uniform distribution of fluorescent tracer is first established in the sample and then a region is photobleached with a strong laser. The diffusion characteristics are determined from the exchange of surrounding tracer with the population of bleached molecules. This technique has been widely applied to studies of cell membranes, which are essentially two-dimensional, and to regions of intracellular cytoplasm (e.g., Luby-Phelps et al., 1986). Chary and Jain (1989) applied the method to whole tissue to measure interstitial convection and diffusion in the rabbit ear and Järnefelt et al. (1988) applied the method to suspensions of erythrocyte ghosts. Several problems limit the use of this technique. The laser beam has a geometry which extends throughout the sample, even when adjusted to give a Gaussian profile, introducing depth problems, and the need for precise alignment of laser and recording optics makes the technique complex and expensive. In addition the intense laser beam needed to photobleach in a brief period can also damage tissue.

Our method has several advantages over those used in the studies mentioned above. First the source is well-defined and closely approximates a point source with an impulse release.

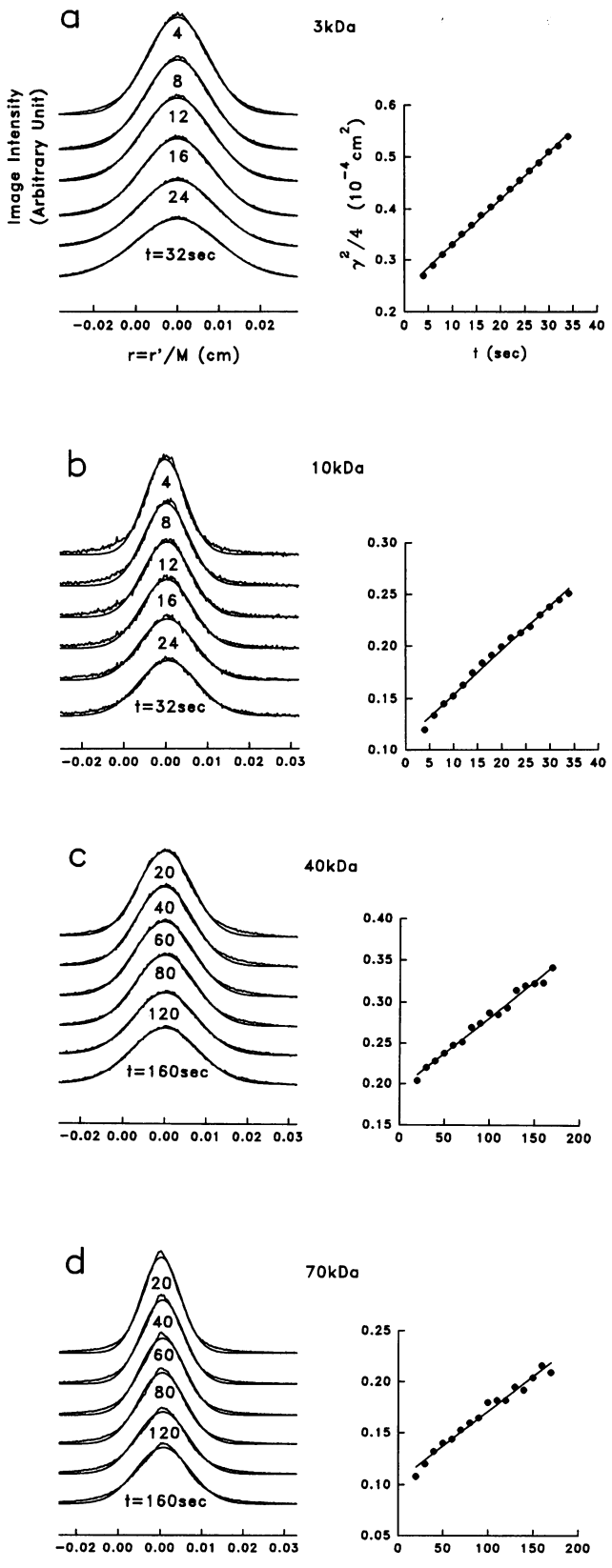


FIGURE 9 Diffusion profiles in cortical slices. These data were obtained as described in Fig. 7 for the agarose gel. The fitting of the theoretical curves to the images is not quite as good as for the agarose, reflecting the greater structural complexity of the brain samples. See text for further discussion.

(In preliminary experiments, not reported here, we have also used an iontophoretic source). Second, none of the studies mentioned have dealt with the problem of out-of-focus molecules which can make varying contributions to the image. Noting that the available theoretical treatments of this problem were inadequate, we developed our own solution (Tao and Nicholson, submitted). Third, because our measurements are made with weak illumination, there is no need to correct for photobleaching. Low illumination is feasible because we are able to introduce a sufficient amount of fluorescent marker using the pressure ejection technique. At the same time, we do not see self-quenching effects at the concentrations employed. A fourth advantage of our method is that it is relatively simple. We used a cooled CCD camera which provided excellent dynamic range and linearity, factors which facilitate quantitative analysis, but less expensive imaging devices could be used with suitable image intensifiers and calibration.

The simplicity of our method does introduce limitations. As presently implemented, the method assumes that the dye molecules diffuse with a spherical distribution about the point source. For the issue which we are presently exploring (the way in which large molecules move in the BEM) this is not a limitation. For the analysis of inhomogeneous diffusion domains, however, the method would require further refinement. We have not taken into account light scattering or absorption. Perhaps the simplest and most convincing argument for assuming these effects to be insignificant with our method, even in brain tissue, is the excellent agreement with earlier data (discussed below) that we obtain for both diffusion coefficient and tortuosity, using the two lower molecular weight dextrans.

## Diffusion in agarose

The diffusion coefficient that we measured in 0.3% agarose gel dissolved in isotonic saline should closely approximate the free diffusion value in the interstitial space of the brain, which in turn should be close to the aqueous value. At the low concentrations of agarose used, we do not believe that the diffusion was significantly hindered. Schantz and Lauffer (1962) indicated that large molecules (other than charged proteins) have their diffusion coefficient reduced by about 3–5% in a 1.5% (w/v) agar gel. This result was substantiated for small cations by Slade et al. (1966) who found that $D^* = D/F$ where $F = 1 + 0.023w$ and $w$ is the weight percent of agar; thus again for a 1.5% agar the measured $D$ would be about 3% less than that in free solution. Schantz and Lauffer also noted that charged proteins are slowed down in agar gels. This was confirmed by Ackers and Steere (1962) and Jain et al. (1990) who showed that the apparent diffusion coefficient of albumin in 2% (w/v) agar gel was about 70% of that in aqueous solution. Since we used essentially neutral carbohydrate molecules and 0.3% agarose gel, these data suggests the error in our measurements of $D$ due to agarose obstruction would be less than 1%.

We now compare the values of $D$ that we obtained for the dextrans in agarose with the values obtained with other methods. One of the most extensive data sets is that of Granath and Kvist (1967) where the molecular weights were derived by gel filtration and light scattering, and the diffusion coefficients by extrapolation from an earlier sedimentation analysis (1958). Since those data were obtained at 20°C we transformed them to 34°C using Einstein's relation which leads to $D_{34} = D_{20}\ (T_{34}/T_{20})(\eta_{20}/\eta_{34})$, where $T$ is the absolute temperature and $\eta$ is the viscosity of water (tabulated in Philippoff, 1963). The data of Granath and Kvist could then be accurately described by the relation $D_{34}\ (\text{cm}^2\ \text{s}^{-1}) = 1.11 \times 10^{-4} \times (M_r)^{-0.48}$ (see Nugent and Jain, 1984a). (It may be noted that simple theoretical considerations (Rubinow, 1975) suggest that $D(M_r)^{1/2} =$ constant for $M_r < 1000$ but $D(M_r)^{1/3} =$ constant for larger molecules, such as those used by Granath and Kvist). The relation that describes the data of Granath and Kvist predicts values for $D_{34}$ of $23.8 \times 10^{-7}\ \text{cm}^2\ \text{s}^{-1}$ for the 3-kDa dextran and $13.3 \times 10^{-7}\ \text{cm}^2\ \text{s}^{-1}$ for the 10-kDa molecule, which are almost identical to those that we measured (Table 1). In contrast the same relation predicts values for $D_{34}$ of $6.86 \times 10^{-7}\ \text{cm}^2\ \text{s}^{-1}$ for the 40-kDa dextran and $5.24 \times 10^{-7}\ \text{cm}^2\ \text{s}^{-1}$ for the 70-kDa dextran. These values are 63% (40 kDa) and 38% (70 kDa) greater than those we obtained. Dextrans are polydisperse, but the quality of the curve fitting (e.g., Fig. 7) does not suggest that this is a factor and it would be peculiar for the distribution of molecular weights to be so biased toward high values. At this time it is not possible to account for the differences in values of $D$ for the two larger dextrans from those derived from the data of Granath and Kvist.

The results that we obtained with agarose gels validate the IOI method. There is almost perfect agreement between our data and those obtained with totally different methods by Granath and Kvist for 3- and 10-kDa dextrans. Because of this agreement, the discrepancies at the higher molecular weights probably can be attributed to physico-chemical factors rather than methodological ones.

For later discussion of the passage of dextrans though the BEM it is useful to have an estimate of the size of the molecules. Conventionally this would entail estimating the Stokes radius from the formula $r_{\text{Stokes}} = RT/(6\pi\eta DN)$, where $R$ is the gas constant and $N$ is Avagadro's number. Use of this formula begs the question of whether the molecules can reasonably be assumed to be spheres. Ogston and Wood (1953) and Granath (1958) both conclude that dextrans become more symmetrical with increase in molecular weight and Luby-Phelps et al. (1986) noted that, although dextrans do not have a well-defined configuration, because they are random coil polymers, their size can be defined statistically by the radius of gyration $r_G = r_{\text{Stokes}}/0.665$. Most authors do calculate the Stokes radius nonetheless. Such a calculation indicates that the 3-, 10-, 40-, and 70-kDa dextrans that we have used have radii of 13, 23, 73, and 81 Å, respectively, based on our values of $D$. If the Granath and Kvist data are used instead for the two larger dextrans then their radii would be 45 and 59 Å.

## Diffusion in cortical slice

The tortuosities, $\lambda$, that we obtained with the 3- and 10-kDa dextrans (1.70 and 1.63, respectively) in the cortical slices are consistent with other types of measurement in various regions of brain and spinal cord (see Nicholson and Phillips (1981) and Nicholson (1993) for reviews of earlier literature). What is unexpected is the larger value of $\lambda$ measured with the two higher molecular weight dextrans. To explore this result further we need to consider the validity of the data.

There have been several recent estimates of $\lambda$ for the cortex using the tetramethylammonium method. The two most detailed studies were by Cserr et al. (1991) who obtained a value of 1.57 for the cortex in the intact, anesthetized rat. The other detailed study by Lehmenkühler et al. (1993), also on the intact neonatal and adult rat concluded that the values of $\lambda$ ranged between 1.51 and 1.65 for different layers and ages. Three other studies obtained lower values for $\lambda$. Lehmenkühler et al. (1985) obtained 1.40 and Nicholson and Rice (1987) obtained 1.34, but these were limited studies. Recently Lundbæk and Hansen (1992) also obtained a $\lambda$ of 1.40. In the latter study the tetramethylammonium method was employed without taking into account the uptake of this small molecule or attempting to fit the falling phases of the diffusion curves; neglecting these factors may lead to an underestimate of $\lambda$, since the time course of the curve is modified by uptake.

The increased values of $\lambda$ seen with the two larger dextrans in the present study is striking, with values of 2.17 and 2.26 for the 40- and 70-kDa dextrans, respectively. As noted above, there is some discrepancy between our values of $D$ and those extrapolated from the data of Granath and Kvist (1958) for the 40- and 70-kDa dextrans, however, if the extrapolated values are used instead of ours for $D$, then the values of $\lambda$ would be even larger, 2.75 and 2.64, respectively. Thus we believe that the increase in hindrance with the larger molecules is real and significant.

Two explanations can be offered for the increased hindrance in the diffusion of the larger molecules. The first is that there is interaction between the carbohydrate branches of the dextrans and similar groups on the surfaces of the brain cells. This explanation is based on the data of Järnefelt et al. (1988) who found a large decrease in apparent diffusion coefficient of dextrans in suspensions of erythrocyte ghosts compared to suspensions of latex spheres. Erythrocytes have a dense carbohydrate layer attached to their outer surface Järnefelt et al. (1988), and it is known that dextrans are retarded in concentrated solutions (Laurent et al., 1976). The density of carbohydrate molecules associated with cells of the brain is unlikely to be as high as those covering erythrocytes, although data is much more sparse (Margolis et al., 1986). Charge interaction cannot account for the increased $\lambda$, because the dextrans are neutral, the charge groups being associated with the dye molecules. A second explanation, which we favor, is that the size of the spaces between cells varies, and that molecules above a certain size are excluded from some intercellular passages. This limiting size can be

approximated. Since 10-kDa dextrans (Stokes radius of 23 Å) are hindered no more than much smaller molecules, the diameter of extracellular space is probably larger than 50 Å. Dextrans of 40 kDa (Stokes radius of either 73 or 45 Å) are more hindered suggesting there are regions that are narrower than 150 Å. It is interesting to note that the popular estimate of the extracellular space diameter is 150–200 Å, although this may be an artifact of conventional fixation for electron microscopy (Schmitt and Samson, 1969).

Somewhat similar constraints have been proposed for diffusion in the brain intracellular microenvironment. Luby-Phelps et al. (1988) studying the intracellular diffusion of dextrans and Ficolls have found that the mobility of the molecules is sharply curtailed above a certain size, which is in the region of $r_G$ = 140 Å for dextrans and $r_G$ = 240 Å for Ficolls. The authors of those studies tentatively attributed their results to the size of the mesh structure of cytoplasm; they also noted that all molecules, including small ones, diffuse at least three times slower than in aqueous solution, suggesting that there is a similar tortuosity in the intracellular microenvironment as in the extracellular.

## Implications for the movement of macromolecules through the brain

There is currently considerable interest in the therapeutic use of large molecules from families of neurotrophic factors to restore function in various neurologic diseases. To be effective, such molecules must be able to reach their targets. While dextrans differ structurally from some of these potential therapeutic compounds, our data do indicate that molecules as large as 70 kDa can pass through the BEM. Significantly, however, our data indicate that certain sites might not be accessible. On the other hand, below some limit between 10 and 40 kDa, molecular diffusion is not restricted any more than that seen with much smaller entities. For particular molecules, however, charge interactions and other forms of more specific binding could greatly hinder movement. For that reason, it is essential to study the behavior of individual molecular species. The results presented here indicate that, so long as a fluorescent label can be attached, our methods can provide such information.

We are grateful to Dr. T. Ebner and colleagues at the University of Minnesota for helping us to get started with this project. Drs. M. Rice, M. Chesler, M. Peréz-Pinzón and J. Cappell offered helpful criticisms of the manuscript. S. Sleet provided technical assistance.
Supported by National Institutes of Health grant NS 28642.

## REFERENCES

Ackers, G. K., and R. L. Steere. 1962. Restricted diffusion of macromolecules through agar gel membranes. *Biochim. Biophys. Acta.* 59:137–149.

Agard, D. A. 1984. Optical sectioning microscopy: cellular architecture in three dimensions. *Annu. Rev. Biophys. Bioeng.* 13:191–219.

Aggarwal, S. J., S. J. Shah, K. R. Diller, and C. R. Baxter. 1989. Fluoresence digital microscopy of interstitial macromolecular diffusion in burn injury. *Comput. Biol. Med.* 19:245–261.

Basser, P. J. 1992. Interstitial pressure, volume, and flow during infusion into brain tissue. *Microvascular Res.* 44:143–165.

Born, M., and E. Wolf. 1986. Principles of Optics, 6th Edition, Pergamon, New York, 808 pp.

Castleman, K. R. 1979. Digital Image Processing. Prentice-Hall, Englewood Cliffs, NJ. pp. 351–360.

Chary, S. R., and R. K. Jain. 1989. Direct measurement of interstitial convection and diffusion of albumin in normal and neoplastic tissues by fluorescence photobleaching. *Proc. Natl. Acad. Sci. USA.* 86:5385–5389.

Cserr, H. F., M. DePasquale, C. Nicholson, C. S. Patlak, K. D. Pettigrew, and M. E. Rice. 1991. Extracellular volume decreases while cell volume is maintained by ion uptake in rat brain during acute hypernatremia. *J. Physiol.* 442:277–295.

Fenstermacher, J. D., and C. S. Patlak. 1975. The exchange of material between cerebrospinal fluid and brain. *In* Fluid Environment of the Brain. H. F. Cserr, J. D. Fenstermacher, and V. Fencl, editors. Academic Press, New York. 201–214.

Fenstermacher, F., and Kaye, T. 1988. Drug "diffusion" within the brain. *Ann. N.Y. Acad. Sci.* 531:29–39.

Fox, J. R., and H. Wayland. 1979. Interstitial diffusion of macromolecules in the rat mesentery. *Microvascular Res.* 18:255–276.

Fuxe, K., and L. F. Agnati, editors. 1991. Volume Transmission in the Brain. Advances in Neuroscience, 1. Raven Press, New York.

Granath, K. A. 1958. Solution properties of branched dextrans. *J. Colloid Sci.* 13:308–328.

Granath, K. A., and B. E. Kvist. 1967. Molecular weight distribution analysis by gel chromatography on Sephadex. *J. Chromatogr.* 28:69–81.

Haugland, R. P. 1992. Handbook of Fluorescent Probes and Research Chemicals, 5th Edition. Molecular Probes, Eugene, OR. 421 pp.

Henry, B. T., J. Adler, S. Hibberd, M. S. Cheema, S. S. Davis, and T. G. Rogers. 1992. Epifluorescence microscopy and image analysis used to measure diffusion coefficients in gel systems. *J. Pharm. Pharmacol.* 44: 543–549.

Hiraoka, Y., J. W. Sedat, and D. A. Agard. 1990. Determination of three-dimensional imaging properties of a light microscope system. Partial confocal behavior in epifluorescence microscopy. *Biophys. J.* 57:325–333.

Jain, R. K., R. J. Stock, S. R. Chary, and M. Rueter. 1990. Convection and diffusion measurements using fluorescence recovery after photobleaching and video image analysis: in vitro calibration and assessment. *Microvasc. Res.* 39:77–93.

Järnefelt, J., T. Laurent, and R. Rigler. 1988. Diffusion of fluorescein-labelled molecules in suspensions of erythrocyte ghosts. *FEBS Lett.* 242: 129–133.

Laurent, C., L. O. Sundelöf, K. O. Wik, and B. Wärmegard. 1976. Diffusion of dextran in concentrated solutions. *Eur. J. Biochem.* 68:95–102.

Lehmenkühler, A., H. Caspers, and U. Kersting. 1985. Relations between DC potentials, extracellular ion activities and extracellular volume fraction in the cerebral cortex with changes on $P_{CO2}$. *In* Ion Measurements in Physiology and Medicine. M. Kessler, D. K. Harrison, and J. Höper, editors. Springer-Verlag, Berlin. 199–205.

Lehmenkühler, A., E. Syková, J. Svoboda, K. Zilles, and C. Nicholson. 1993. Extracellular space parameters in the rat neocortex and subcortical white matter during postnatal development determined by diffusion analysis. *Neuroscience.* 55:339–351.

Luby-Phelps, K. 1989. Preparation of fluorescently labeled dextrans and Ficolls. *In* Methods in Cell Biology. Y. L. Wang and D. L. Taylor, editors. Academic Press, San Diego. 59–73.

Luby-Phelps, K., P. E. Castle, D. L. Taylor, and F. Lanni. 1987. Hindered diffusion of inert tracer particles in the cytoplasm of mouse 3T3 cells. *Proc. Natl. Acad. Sci. USA.* 84:4910–4913.

Luby-Phelps, K., D. L. Taylor, and F. Lanni. 1986. Probing the structure of cytoplasm. *J. Cell Biol.* 102:2015–2022.

Luby-Phelps, K., F. Lanni, and D. L. Taylor. 1988. The submicroscopic properties of cytoplasm as a determination of cellular function. *Annu. Rev. Biophys. Biophys. Chem.* 17:369–396.

Lundbæk, J. A., and A. J. Hansen. 1992. Brain interstitial volume fraction and tortuosity in anoxia—evaluation of the ion-selective micro-electrode method. *Acta Physiol. Scand.* 146:473–484.

Margolis, R. U., D. A. Aquino, M. M. Klinger, J. A. Ripellino, and R. K. Margolis. 1986. Structure and localization of nervous tissue proteoglycans. *Ann. N.Y. Acad. Sci.* 481:46–54.

McBain, C. J., S. F. Traynelis, and R. Dingledine. 1990. Regional variation of extracellular space in the hippocampus. *Science (Wash. DC).* 249: 674–677.

Nakamura, Y., and H. Wayland. 1975. Macromolecular transport in cat mesentery. *Microvasc. Res.* 9:1–21.

Nicholson, C. 1979. Brain cell microenvironment as a communication channel. *In* The Neurosciences Fourth Study Program. F. O. Schmitt and F. G. Worden, editors. MIT Press, Cambridge. 457–476.

Nicholson, C. 1985. Diffusion from an injected volume of a substance in brain tissue with arbitrary volume fraction and tortuosity. *Brain Res.* 333:325–329.

Nicholson, C. 1992. Quantitative analysis of extracellular space using the method of $TMA^+$ iontophoresis and the issue of $TMA^+$ uptake. *Can. J. Physiol. Pharmacol.* 70(Suppl.):S314–S322.

Nicholson, C. 1993. Ion-selective microelectrodes and diffusion measurements as tools to explore the brain cell microenvironment. *Neurosci. Methods.* 48:199–213.

Nicholson, C., J. A. Miyan, K. T. Potter, R. Williamson, and N. J. Abbott. 1993. Diffusion properties of the microenvironment of cephalopod brain. *In* Cephalopod Neurobiology. N. J. Abbott, R. Williamson, and L. Maddock, editors. Oxford University Press, Oxford. In press.

Nicholson, C., and J. M. Phillips. 1981. Ion diffusion modified by tortuosity and volume fraction in the extracellular microenvironment of the rat cerebellum. *J. Physiol.* 321:225–257.

Nicholson, C., J. M. Phillips, and A. R. Gardner-Medwin. 1979. Diffusion from an iontophoretic point source in the brain: role of tortuosity and volume fraction. *Brain Res.* 169:580–584.

Nicholson, C., and M. E. Rice. 1986. The migration of substances in the neuronal microenvironment. *Ann. N.Y. Acad. Sci.* 481:55–71.

Nicholson, C., and M. E. Rice. 1987. Calcium diffusion in the brain cell microenvironment. *Can. J. Physiol. Pharmacol.* 65:1086–1091.

Nugent, L. J., and R. K. Jain. 1984a. Extravascular diffusion in normal and neoplastic tissues. *Cancer Res.* 44:238–244.

Nugent, L. J., and R. K. Jain. 1984b. Plasma pharmocokinetics and interstitial diffusion of macromolecules in a capillary bed. *Am. J. Physiol.* 246:H129-H137.

Ogston, A. G., and E. F. Woods. 1953. Molecular configurations of dextrans in aqueous solutions. *Nature (Lond.).* 171:221–222.

Paxinos, G., and Watson, C. 1986. The Rat Brain in Stereotaxic Coordinates. Academic Press, San Diego. 119 plates.

Philippoff, W. 1963. Viscosity of liquids. *In* American Institute of Physics Handbook. D. W. Gray, editor. McGraw-Hill, New York. 2-179–2-184.

Press, W. H., B. P. Flannery, S. A. Teukolsky, and W. T. Vettterling. 1986. Numerical Recipes. Cambridge University Press, Cambridge.

Rice, M. E., Y. C. Okada, and C. Nicholson. 1993. Anisotropic and heterogeneous diffusion in the turtle cerebellum: implications for volume transmission. *J. Neurophysiol.* In press.

Rice, M. E., and Nicholson, C. 1991. Diffusion characteristics and extracellular volume fraction during normoxia and hypoxia in slices of rat neostriatum. *J. Neurophysiol.* 65:264–272.

Rubinow, S. I. 1975. Introduction to Mathematical Biology. Wiley, New York. 210–211.

Schantz, E. J., and M. A. Lauffer. 1962. Diffusion measurements in agar gel. *Biochemistry.* 1:658–663.

Schmitt, F. O. 1984. Molecular regulators of brain functioning: a new view. *Neuroscience.* 13:991–1001.

Schmitt, F. O., and F. E. Samson. 1969. The brain cell microenvironment. *Neurosci. Res. Prog. Bull.* 7:277–417.

Slade, A. L., A. E. Cremers, and H. C. Thomas. 1966. The obstruction effect in the self-diffusion coefficients of sodium and cesium in agar gels. *J. Phys. Chem.* 70:2840–2844.

Stokseth, P. A. 1969. Properties of a defocused optical system. *J. Optical Soc. Am.* 59:1314–1321.

Svoboda, J., and E. Syková. 1991. Extracellular space volume changes in the rat spinal cord produced by nerve stimulation and peripheral Injury. *Brain Res.* 560:216–224.

Tao, L., and C. Nicholson. 1992. Quantitative optical imaging of the diffusion of dextrans of different molecular weights in rat cerebral cortex. *Soc. Neurosci. Abstr.* 18:967.

Thoenen, H., and Y. A. Barde. 1980. Physiology of nerve growth factor. *Physiol. Rev.* 60:1284–1335.

Wiederhielm, C. A., M. L. Shaw, T. H. Kehl, and J. R. Fox. 1973. A digital system for studying interstitial transport of dye molecules. *Microvasc. Res.* 5:243–250.

Yae, H. D., S. A. Elias, and T. J. Ebner. 1992. Deblurring of 3-dimensional patterns of evoked rat cerebellar cortical activity: a study using voltage-sensitive dyes and optical sectioning. *J. Neurosci. Methods.* 42:195–209.